Cement and Concrete Composites 142 (2023) 105186

Contents lists available at ScienceDirect

Cement and Concrete Composites

journal homepage: www.elsevier.com/locate/cemconcomp

Investigation on the influential mechanism of FA and GGBS on the properties of CO_2-cured cement paste

Pingping He [a,b,c], Sarra Drissi [a,b,c,d], Xiang Hu [a,b,c,**], Jianhui Liu [a,b,c], Caijun Shi [a,b,c,e,*]

[a] Key Laboratory for Green & Advanced Civil Engineering Materials and Application Technology of Hunan Province, College of Civil Engineering, Hunan University, Changsha, 410082, PR China
[b] International Science Innovation Collaboration Base for Green & Advanced Civil Engineering Materials of Hunan Province, Hunan University, Changsha, 410082, PR China
[c] Key Laboratory of Building Safety and Energy Efficiency of the Ministry of Education, Hunan University, Changsha, 410082, PR China
[d] Department of Civil Engineering and Energy Technology, Faculty of Technology, Art and Design, Oslo Metropolitan University, PO box 4 St. Olavs plass, Oslo, NO-0130, Norway
[e] Department of Civil Engineering, The University of British Columbia, 6250 Applied Science Lane, Vancouver, BC Canada, V6T 1Z4, Canada

ARTICLE INFO

Keywords:
CO_2 curing
Microstructure
Porosity
Compressive strength
Mortar

ABSTRACT

In the present work, the synergetic effect of fly ash (FA) and ground granulated blast furnace slag (GGBS) on the early compressive strength and microstructure development of CO_2-cured mortars was investigated. A rim of several micrometers was found around carbonated cement particles, which contained not only silica-rich gel but also crystal calcium carbonate. The calcium carbonate formed around the cement particles were surrounded by an amorphous layer of around 3 nm, while no layers were observed around the calcite formed on FA or GGBS particles. The calcite formed on FA particles were hexagonal plate shaped, while the one on GGBS particles were rhombohedral shaped. The use of FA resulted in the increase of crystal size and crystallinity of calcite, while GGBS decreased the crystal size of calcite. The incorporation of FA and GGBS increased the calcite content and polymerization of silica-rich gel. However, this didn't result in a higher compressive strength. This was due to the looser microstructure and nanopores within the carbonation products compared to the pure ordinary Portland cement sample. The compressive strength of the ternary binder system showed linear relationship with capillary pores and the crystal size of calcite. Moreover, the effect of GGBS on the compressive strength reduction was more obvious than that of FA.

1. Introduction

Over the last few decades, research efforts have been made on the carbon capture and storage techniques. Among these techniques, CO_2 curing of concrete is considered to be an effective way for CO_2 utilization. During this accelerated curing process, the anhydrous cement clinker minerals and parts of hydrate products including calcium hydroxide and C–S–H can be carbonated as follows [1]:

$$3\text{CaO} \bullet SiO_2 + 3CO_2 + nH_2O \rightarrow SiO_2 \bullet nH_2O + 3CaCO_3 \quad (1)$$

$$2\text{CaO} \bullet SiO_2 + 2CO_2 + nH_2O \rightarrow SiO_2 \bullet nH_2O + 2CaCO_3 \quad (2)$$

$$\text{Ca(OH)}_2 + CO_2 \rightarrow CaCO_3 + H_2O \quad (3)$$

$$xCaO \bullet ySiO_2 \bullet nH_2O + xCO_2 \rightarrow xCaCO_3 + ySiO_2 \bullet nH_2O \quad (4)$$

Besides, other clinker minerals such as C_3A and C_4AF can also react with CO_2 at limited reaction degree [2,3]. With the thermodynamically stable $CaCO_3$ and fast early strength development of CO_2-cured cement-based materials, CO_2 curing offers a prospective way for CO_2 sequestration and utilization in the concrete industry. Besides, different from traditional steam curing, CO_2 curing is beneficial to the durability of concrete [4] and the reduction of energy consumption [5].

Supplementary cementitious materials (SCMs), are used to partially

* Corresponding author. Key Laboratory for Green & Advanced Civil Engineering Materials and Application Technology of Hunan Province,College of Civil Engineering, Hunan University, Changsha, 410082, PR China.
** Corresponding author. International Science Innovation Collaboration Base for Green & Advanced Civil Engineering Materials of Hunan Province, Hunan University, Changsha, 410082, PR China.
E-mail addresses: xiang.hu@hnu.edu.cn (X. Hu), cshi@hnu.edu.cn (C. Shi).

https://doi.org/10.1016/j.cemconcomp.2023.105186
Received 13 February 2023; Received in revised form 19 April 2023; Accepted 19 June 2023
Available online 19 June 2023

Table 1
Chemical compositions (%) of cementitious components.

	CaO	SiO_2	Al_2O_3	Fe_2O_3	MgO	f-CaO	K_2O	SO_3	Na_2O
PC	62.13	18.93	4.19	3.39	1.82	0.50	0.66	3.16	0.24
FA	5.67	46.43	32.31	7.95	0.73	/	1.63	1.02	0.877
GGBS	40.11	29.18	17.56	0.56	8.94	/	0.56	2.50	0.294

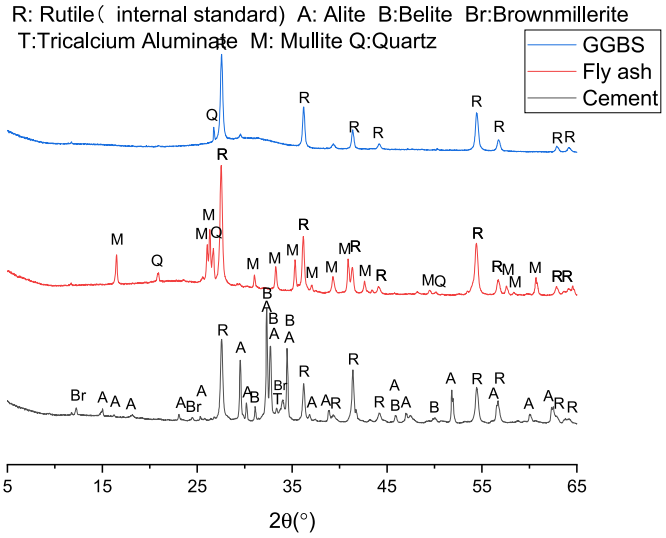

Fig. 1. XRD patterns of the cementitious components.

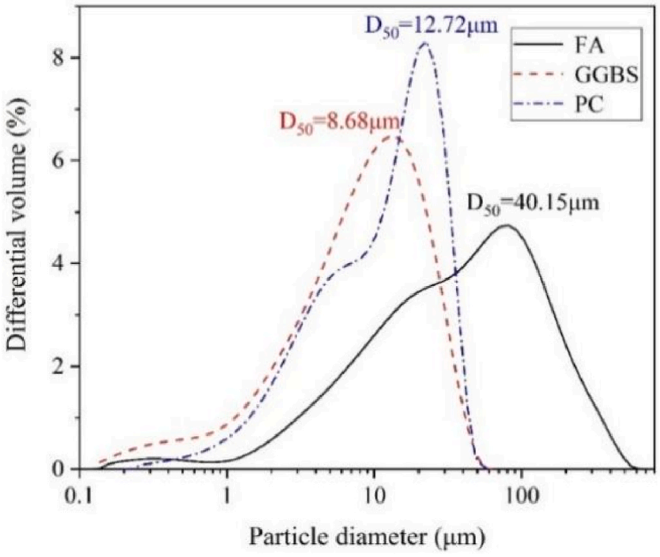

Fig. 2. Particle size distributions of the cementitious components.

replace cement to decrease the content of cement and lower the CO_2 emissions [6] such as fly ash (FA) and granulated grounded blast furnace slag (GGBS). On the other hand, the incorporation of SCMs can improve the long-term durability of concrete such as chloride migration resistance [7] and acid resistance [8]. Generally, the addition of SCMs always results in the decrease of cement clinker and the formed calcium hydroxide. Thus, the effects of early CO_2 curing on cement-based materials may be varied when it is blended with SCMs.

The research on blended cement has mainly focused on the carbonation of hardened cement and concrete. During the carbonation process, hydration products are carbonated such as calcium hydroxide and C–S–H gel. However, this reaction is not likely to happen during CO_2 curing. As mentioned above, it is mainly anhydrous cement clinkers that undergo carbonation during CO_2 curing process [9] such as C_3S and C_2S. Zhang et al. [10,11] compared the carbonation curing process and carbonation degree of concrete with and without FA. They found that FA could facilitate the CO_2 uptake even though it decreased the ultimate compressive strength of CO_2-cured concrete. Qin et al. [12] investigated the compressive strength and CO_2 uptake of CO_2-cured mortars incorporating FA, GGBS, and limestone. It was found that the addition of 20% SCMs decreased the compressive strength but increased the CO_2 uptake. Wang et al. [13] used CO_2 curing to treat the surface of wet-mixed cement specimens incorporating SCMs to decrease the penetrability. However, more extensive and systematic investigations are still needed to fully understand the role and influencing mechanisms of SCMs on the CO_2 curing of cement-based materials.

Generally, studies on the CO_2 curing of blended cement focused on the performance of cement concrete incorporating a single type of SCM. However, there is an increased interest in replacing cement by more than one type of SCM in order to further decrease the content of cement in concrete. Therefore, investigating the synergetic effect of hybrid SCMs on the CO_2 cured concrete is of great interest for application of industrial waste and CO_2 curing. Besides, the lack of knowledge about the evaluation of the microstructure evolution makes it difficult to investigate the effects of CO_2-curing on the microstructure, morphology, and mechanical properties of the formed products in the blended concrete. Therefore, the objectives of this research include: 1) assessing the synergetic influences of GGBS and FA on the carbonation degree, compressive strength and pore size distribution of dry-mixed cement-GGBS-FA ternary mortars subjected to CO_2 curing; 2) investigating the morphology and crystallinity of the carbonation products; 3) understanding the underlying mechanisms by which GGBS and FA impact the CO_2 curing process and the microstructure of CO_2-cured mortars.

2. Materials and testing methods

2.1. Materials

Portland cement (PC, PI 42.5), according to the specifications of the Chinese standard GB 8076-2008 [14], class F FA and GGBS were used in this study. The chemical compositions of cementitious components obtained by PANalytical Axios X-ray fluorescence are listed in Table 1. 20% of rutile was used as internal standard to quantify the mineral compositions of raw materials based on XRD patterns as shown in Fig. 1. It can be seen that the phase composition of the anhydrous PC is mainly alite (61.6%), belite (14.5%), brownmillerite (10.0%) and tricalcium aluminate (4.0%). Almost no amorphous phases were observed in PC. The FA is composed of mullite (31.3%), quartz (4.4%) and amorphous phase (63.6%), while GGBS consists mainly of amorphous phases (98.3%). The particle size distribution of cementitious components, obtained by Microtrac S3500 laser particle size analyzer, are shown in Fig. 2. River sand, with a fineness modulus of 2.9 and a maximum size of 2.5 mm, was used as fine aggregate.

2.2. Mixture proportions

The binder compositions of cement mortars were designed based on the simplex-centroid mixture design [15]. Thus, the experimental results could be analyzed by the following linear model (Eq. (5)). According to the literature, this design method is a good prediction tool to evaluate and optimize the mixture proportion of cement-based materials. Several

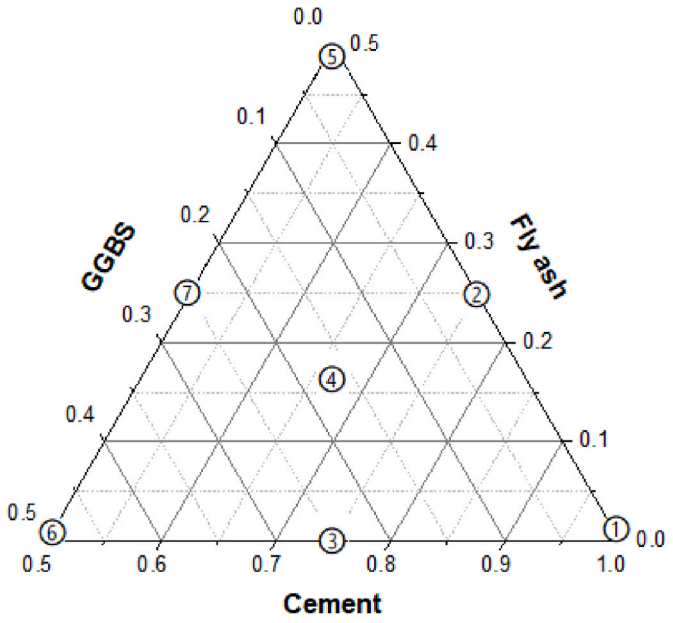

Fig. 3. Composition design of ternary mortar system (mass ratio).

Table 2
Weight proportions of cementitious components in ternary system.

No.	PC	FA	GGBS
C1	1	0	0
C2	0.75	0.25	0
C3	0.75	0	0.25
C4	0.667	0.167	0.167
C5	0.5	0.5	0
C6	0.5	0	0.5
C7	0.5	0.25	0.25

studies reported that the difference between the experimental values and the model's predicted values are small and unbiased ($R^2 \geq 0.9$) [16–18]:

$$Y = \beta_1 X_1 + \beta_2 X_2 + \beta_3 X_3 + \beta_{12} X_1 X_2 + \beta_{13} X_1 X_3 + \beta_{23} X_2 X_3 + \beta_{123} X_1 X_2 X_3 \quad (5)$$

where Y = response; βi = parameter to be estimated. X_1, X_2, X_3 = mass proportions of PC, FA, and GGBS, respectively. $\sum_{i=1}^{3} x_i = 1$.

The ranges of mass proportion were: $0.5 \leq X_1 \leq 1$, $0 \leq X_2 \leq 0.5$, and $0 \leq X_3 \leq 0.5$. The binder compositions of samples are schematized in Fig. 3 and listed in Table 2.

2.3. Specimen preparation

The fabrication of the mortar specimens simulated the production process of brick and block in the factory. As such, the dry powder with water to binder ratio of 0.25 and PC to fine aggregate ratio of 1:2 was compacted into cylinders with a diameter of 25 mm and a height of 35 mm using a pressure of approximately 10 MPa. In certain cases, the use of paste powder is deemed more precise for microstructural examination. Hence, in this study, paste samples were produced to facilitate the microstructural and phase analysis. Similar to mortar, the paste, with a water to binder ratio of 0.18, was compacted into cylinders with a diameter of 25 mm and a height of 12 mm. The paste and mortar samples were demoulded immediately after casting. In order to have an equal water to binder ratio of 0.18 as that of the paste, the mortar samples were pre-conditioned firstly while the pastes were subjected directly to CO_2 curing. The residual water to binder ratio of 0.18 was selected in this study to ensure a higher carbonation degree as recommended by He et al. [19].

2.4. Curing regimes

2.4.1. Pre-conditioning

The mortar samples were placed in an airy environment for pre-conditioning for around 3 h until the residual water to binder ratio $(W/B)_e$ calculated by Eq. (6) reached around 0.18.

$$(W/B)_e = \frac{\left(1 - \frac{W_0 - W_f}{W}\right) W}{B} \quad (6)$$

Where W_0 and W_f are the mass of the specimens before and after pre-conditioning; W is the mass of water in the mortar specimens before pre-conditioning, and B is the mass of binder in the mortar specimens.

2.4.2. CO_2 curing

Paste and mortar specimens were placed in a CO_2 curing chamber for 3 h. The gas pressure of pure CO_2 was kept at 0.2 MPa. The CO_2 curing setup and detailed information can be found in our previous study [19].

2.5. Test methods

2.5.1. Compressive strength

A pressure measurement instrument (TYA-300B) was used to measure the compressive strength of mortars right after CO_2 curing at a loading rate of 0.6 kN/s. The average value of three specimens were calculated and presented.

2.5.2. X-ray diffraction (XRD) examination

The paste specimens were firstly crushed and then immersed in ethyl alcohol for 24h to stop hydration. Following this, they were dried in a vacuum drying oven for 48h, grinded with a mortar, and sieved through a 75 μm mesh. The XRD examination was conducted on Rigaku R-axis Spider working with Cu Kα radiation within the 2θ range of 5–65° using step size of 0.02° and a rate of 1.2°/min. Rietveld-XRD method were performed using HighScore program to calculate the individual crystalline and amorphous phases. 20% of rutile was used as the internal standard. The amorphous content was calculated based on the following equation:

$$\%A_m = \left(1 - \frac{W_s}{R_s}\right)(1 - W_s)^{-1} \times 10^2 \quad (7)$$

Where W_s is the weighted concentration of rutile; R_s is Rietveld analyzed concentration of rutile.

2.5.3. Thermalgravimetric (TG) analysis

TG measurements were performed on powdered paste samples using a 409 PC simultaneous thermal analyzer at a heating rate of 10 °C/min from 20 °C to 1000 °C under a nitrogen atmosphere. The powdered samples were prepared as explained above (section 2.5.2). Eqs. (8) and (9) were used to calculate the CO_2 uptake and carbonation degree, respectively:

$$CO_2(wt\%) = \frac{\Delta m_{CO_2}}{m_{1000°C}} \times 100 \quad (8)$$

Where $m_{1000°C}$ is the residual mass of the sample after 1000 °C for TG analysis, Δm_{CO_2} is the mass loss of the sample between 550 °C and 1000 °C; $CO_2(wt\%)$ is the percentage of CO_2 uptake by the sample.

$$\alpha = \left(\frac{W_{con}}{W_{max}}\right) \times 100\% \quad (9)$$

Where W_{con} is the CO_2 uptake of specimens, W_{max} is the theoretical maximum CO_2 uptake of PC, which was calculated using Eq. (10) [20]:

$$W_{max} = 0.785([CaO] - 0.7[SO_3]) + 1.091[MgO] + 1.420[Na_2O] + 0.935[K_2O] \quad (10)$$

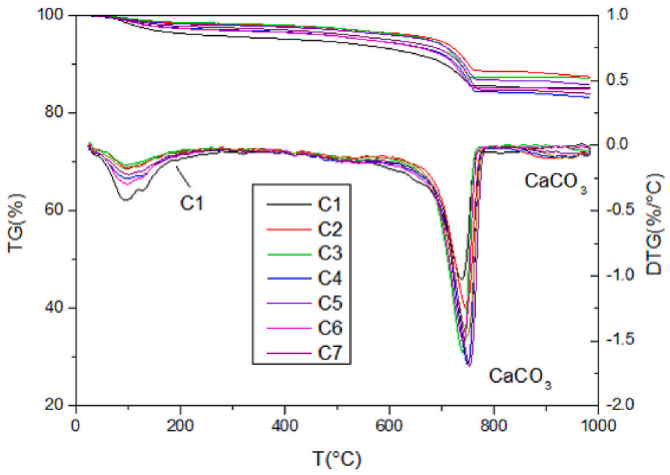

Fig. 4. TG-DTG curves of pastes.

Where [CaO], [SO_3], [MgO], [Na_2O] and [K_2O] are the mass fractions of these oxides in PC.

2.5.4. FTIR

Cement pastes were crushed, immersed in ethyl alcohol for 24h to stop hydration, and then dried in a vacuum drying oven at 40 °C for 48h. FTIR spectra were obtained with a Thermo-Scientific IS10 FTIR instrument. The pellets were prepared by a constant sample to KBr ratio of 1:100. The FTIR spectra recorded in the range 4000 to 400 cm^{-1} were obtained at 2 cm^{-1} resolution.

2.5.5. Proton nuclear magnetic resonance examination

MAG-MED proton nuclear magnetic resonance spectroscopy (^1H NMR) PM-1030 (Jiangsu Magma Medical Technology Co., Ltd, China) operated at 10 MHz was employed to investigate the pore size distribution of the paste specimens. The 90° pulse length was 100 ns and the intrinsic spectrometer dead time was less than 15 ms. Carr-Purcell-Meiboom-Gill (CPMG) measurements were applied with a 30 mm probe to measure the T2 relaxation time. The relaxometry data was analyzed by applying an inverse Laplace transform algorithm. The number of scans was 64, and the recycle delay was 7s with a sampling interval of 0.08 ms. The CO_2-cured paste samples were firstly immersed into distilled water for 10h at a vacuum pressure of 0.1 MPa. Then, the samples were taken out from water, wiped off the water on the surface and placed into the magnet coil with a diameter of 30 mm for NMR test. The pore size (r) distribution was calculated based on the equation Eq. (11) [21,22]:

$$\frac{1}{T_2} \approx \frac{1}{T_{2,surf}} = \rho_2 \left(\frac{S}{V}\right)_{pore} = F_S \times \frac{\rho_2}{r} \tag{11}$$

Where T_2 is the transversal relaxation time of water; $T_{2,surf}$ is the transversal relaxation time due to the surface relaxation; $(S/V)_{pore}$ is the specific surface area of pore; F_s is geometrical factor, $F_s = 2.0$ for cylinder pore; ρ_2 is the surface relaxivity, which was assumed to be 50 μm/s [22].

2.5.6. Scanning electron microscope (SEM) examination

Fractured mortar samples with a particle size of less than 5 mm collected after compressive strength test were stored in ethyl alcohol for 24 h to stop hydration. Then, they were placed in a vacuum drying oven for 48h. After drying, the samples were examined using Phenom LE SEM. This system was configured to take backscatter electron images (BSE) and to carry out EDS (energy-dispersive X-ray spectroscopy) element analysis. For BSE examination, dried samples were stabilized by vacuum impregnation with a low viscosity epoxy resin, polished with 5, 2.5, and 1 μm diamond paste, and then carbon coated. The microscope was operated at 10 kV accelerating voltage.

2.5.7. Transmission electron microscopy (TEM)

TEM data was collected on powdered paste samples, prepared as detailed in section 2.5.2 using Thermofisher talos f200i equipped with Bruker 6T/100RT EDS system. Before testing, the finely ground powder was dispersed in acetone solution. A droplet was extracted from the dilute suspension and deposited on a grid with carbon film.

3. Results

3.1. Carbonation degree

The results of TG-DTG analysis for cement pastes with early CO_2 curing are presented in Fig. 4. Two main peaks were observed in the differential thermalgravimetric (DTG) curves. The first peak at approximately 100 °C is attributed to the dehydration of silica-rich gel, and the second peak at approximately 750 °C is attributed to the decomposition of calcium carbonate. The decomposition peak of C2, C4, C5 was higher than that of C1, C3 and C7, which indicated that the incorporation of FA improved the crystallinity of calcium carbonate [23]. The intensity of the small peak around 900 °C in C2, C4 and C5 was also higher than that in C1, C3 and C7. Therefore, it is suggested that this small peak was also due to the decomposition of calcium carbonate.

Table 3 summarizes the calcium carbonate content of different samples based on the TG result. The calcium carbonate content increased due to the incorporation of FA or GGBS. The CO_2 uptake and carbonation degree of different samples normalized by the weight of PC was calculated and presented in Table 3. It can be seen that the incorporation of FA and GGBS increased the CO_2 uptake and the carbonation degree. The CO_2 uptake and carbonation degree of reference cement paste (C1) were 9.53% and 19.06%. However, these values increased to 11.25% and 45%, respectively, when 25% FA and 25% GGBS (C7) were used.

3.2. Compressive strength

The compressive strength of mortars after 3h of CO_2 curing was also shown in Table 3. The compressive strength of cement mortar without

Table 3
Analysis results of specimens.

No.	Mass loss (%)		CO_2 uptake (%)	Carbonation degree (%)	Compressive strength (MPa)	Crystal size (nm) of calcite	porosity (%) of pastes	Percentage of pores (%)	
	25 °C–200 °C	600 °C–1000 °C						Gel pores (<200 nm)	Capillary pores (>200 nm)
C1	4.11	9.14	9.53	19.06	30.4	29.4	16.4	6.5	9.9
C2	2.48	12.35	12.66	33.77	20.3	30.9	15.4	2.8	12.6
C3	2.64	10.73	11.02	29.39	12.6	30.7	29.0	8.2	20.8
C4	2.33	12.11	12.40	37.18	15.9	30.7	22.6	6.0	16.6
C5	1.48	9.67	9.82	39.26	10.1	35.3	15.0	4.0	11.0
C6	1.38	11.20	10.34	41.37	10.1	28.8	33.4	10.0	23.4
C7	1.87	11.04	11.25	45.00	10.5	33.2	20.3	8.3	12.0

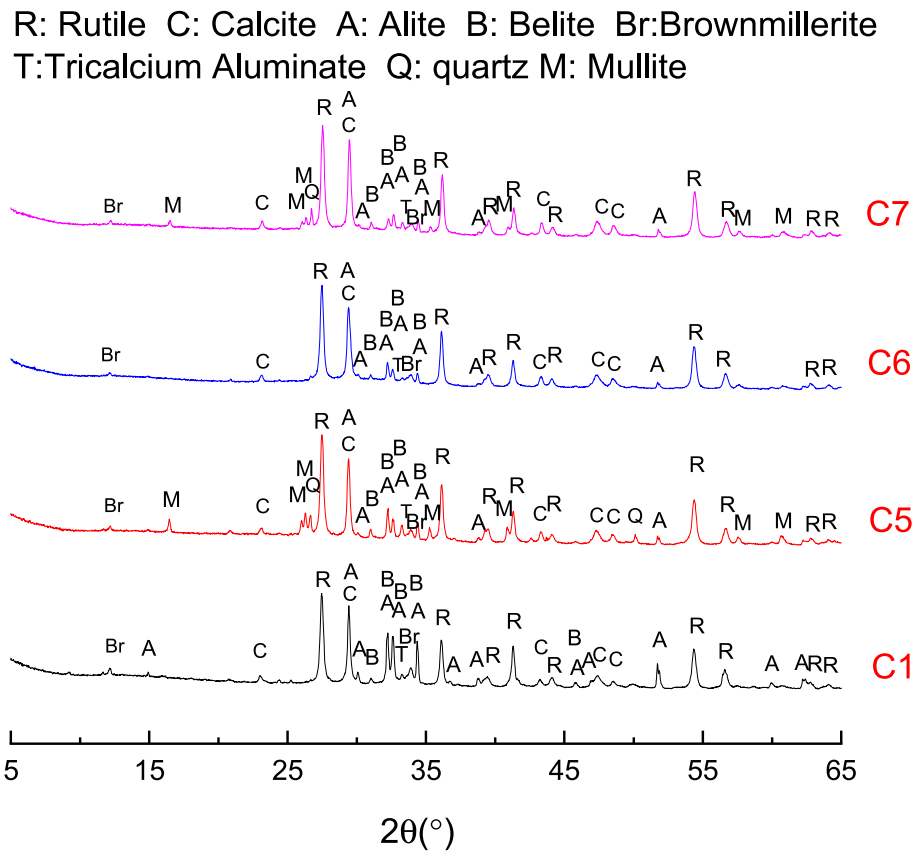

Fig. 5. The XRD patterns collected on the PC-FA-GGBS pastes.

Table 4
Mineralogical compositions (%) of pastes.

No.	Alite	Belite	C_3A	Brownmillerite	Calcite	Quartz	Mullite	Am
PC	61.6	14.5	4.0	10.0	0	0.2	0	0
FA	0	0	0	0	0	4.4	31.3	63.6
GGBS	0	0	0	0	0.8	0.6	0	98.3
C1	23.0	3.9	2.0	4.7	10.9	0	0	51.1
C2	11.3	1.6	0.8	3.8	18.8	0.4	6	56.7
C3	10.2	1.2	0.6	3.6	16.5	0	0	67
C4	8.3	1	0.7	3.1	19.4	0.5	3.7	62.2
C5	7.8	0.7	0.6	2.3	12.8	1.7	15.6	57.3
C6	4.6	0.4	0.3	2.3	18.5	0	0	73
C7	6.4	1.1	0.5	2.3	17.4	1.3	7.6	63.1

any SCMs was 30.4 MPa. However, the incorporation of FA and GGBS decreased substantially the strength. Specifically, adding 25% of FA or GGBS resulted in a strength of 20.3 MPa and 12.6 MPa, respectively. The strength further decreased to 10.1 MPa when 50% of FA or GGBS was used.

3.3. XRD

Fig. 5 shows the XRD patterns of different related cement pastes. The main crystalline carbonation product in control paste (C1) was calcite. A certain amount of alite was also detected, indicating that some cement particles remained uncarbonated. When adding FA or GGBS (samples C5, C6, C7), the main calcium carbonate was still calcite.

The main mineralogical compositions in raw materials and pastes subjected to CO_2 curing are summarized in Table 4. Note that the goodness of fit of Rietveld refinement was lower than 2. The PC particles contained mainly alite and belite. After CO_2 curing, the contents of these two components in C1 decreased significantly due to the reaction shown in Eqs. (1) and (2). Calcite was the main carbonation product in C1 and its content was about 10.9%. A certain amount of amorphous phase, about 51.1%, was detected in C1, which was due to the formation of silica gel and C–S–H gel with a low Ca/Si ratio [24,25]. With the incorporation of FA and GGBS, the calcite and amorphous phase content increased. It is worth mentioning that the amorphous phase comprised that which was present in the raw FA and GGBS.

The mean crystal size of calcite was calculated according to the Scherrer formulation [26]:

$$D = \frac{0.89\lambda}{\beta \bullet cos\ \theta} \tag{12}$$

Where D is the crystal size, λ is the wavelength of Cu Kα (0.15148 nm), β is the full width at half maximum (FWHM), and θ is the diffraction angle.

Table 3 shows the crystal size of calcite in different mixtures. For most mixtures, the incorporation of FA increased the crystal size of calcite whereas an increase of GGBS content (above 25%) decreased the crystal size of calcite. This will be discussed in detail in the following sections.

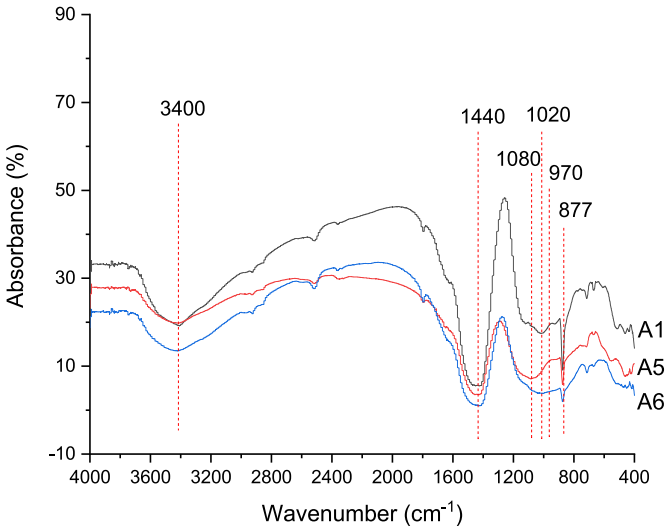

Fig. 6. FTIR spectra of A1, A5 and A6 after CO_2 curing.

3.4. FTIR

Fig. 6 shows the FTIR spectra of cement paste with different mixtures. These spectra contain mainly three wide and intense bands. The peaks at around 3400 cm^{-1}, 1440 cm^{-1} and 877 cm^{-1} are due to the symmetric stretching vibration of hydroxyl group from water molecule [26], antisymmetric stretching and in-plan bending vibration of $CO3^{2-}$ ions [27] respectively. Wavenumber range of 800-1200 cm^{-1} is characteristic of Si–O–Si(Al) in silica-rich phase. The Si–O stretching of the vibrations of Q0, Q1 and Q2, Q3 and Q4 are represented by the peaks at around 850 cm^{-1}, 970-1040 cm^{-1} and 1073-1150 cm^{-1}, respectively. C–S–H gel mainly contains Q1 and Q2 tetrahedra, while silica gel mainly contains Q3 and Q4 tetrahedra [28]. The peak at higher wave number corresponds to higher degree of polymerization of Si [29]. The combination of similar absorptions of Si–O–Si(Al) results in overlap and broad peak from 750 cm^{-1} to 1250 cm^{-1}. Therefore, deconvolution is performed with the Peakfit software as shown in Fig. 7 to assign and quantify the phases contributing and the results are summarized in Table 5. The fit was performed with Gaussian functions and the regression coefficient (R^2) was higher than 0.99. The area ratio of (Q3+Q4)/(Q1+Q2) was calculated to evaluate the polymerization degree of silica-rich phase. Portland cement contained mainly two peaks at 940 cm^{-1} and 1150 cm^{-1}. Carbonated cement (Fig. 7(d)) contained a certain amount of Q1, Q2, Q3 and Q4, but the main peak shift to higher wavenumber and the polymerization degree was increased from 0.47 to 1.34. This indicated the existence of C–S–H gel and silica gel with higher polymerization compared to cement. The peak in raw FA showed higher wavenumber compared to Portland cement. After carbonation, the Q1 and Q2 contents in A5 was much lower than that in A1 and the main peak was Q3. The polymerization degree of A5 was 15.23, which was much higher than A1. This increase was partly due to the higher polymerization degree of the raw FA when compared to Portland cement. However, the primary reason for this increase was the ability of FA to enhance the carbonation and promote the formation of silica gel. GGBS mainly contained one peak at 965 cm^{-1}, which corresponded to the vibration of Q2. For the cement paste incorporating GGBS (A6), the main peaks were located at 1039 cm^{-1}, and the polymerization of silica was 7.75, which was much higher than that of A1. This indicates that the addition of GGBS improved the carbonation and the polymerization of silica phase.

Table 5
Deconvolution of FTIR spectra between 750 and 1250 cm^{-1}.

No.	Q0	Q1	Q2	Q3	Q4	(Q3+Q4)/(Q1+Q2)
Cement	11.49	45.58	14.28	3.27	24.91	0.47
A1	4.22	22.59	16.11	30.35	21.8	1.34
FA			32.78	35.55	31.67	2.05
A5	7.63	5.31		66.87	13.99	15.23
GGBS	3.92	2.49	73.28	20.29		0.27
A6	16.22	9.06		58.55	11.67	7.75

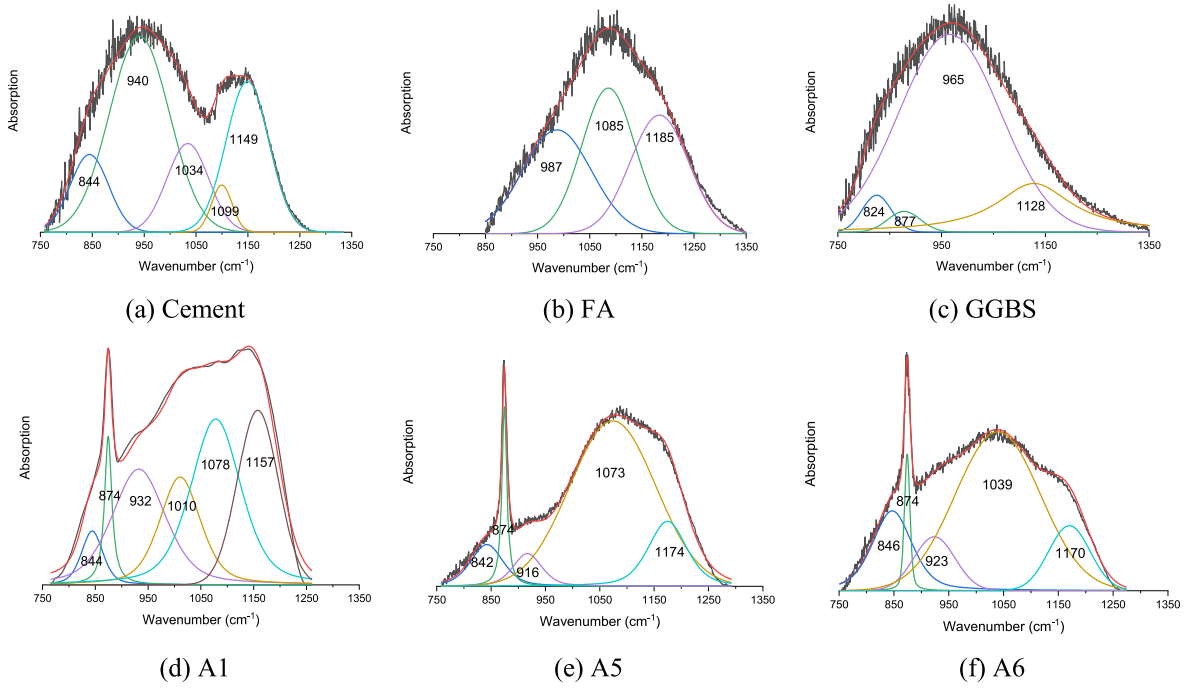

Fig. 7. Deconvoluted FTIR spectra of raw materials and CO_2-cured paste.

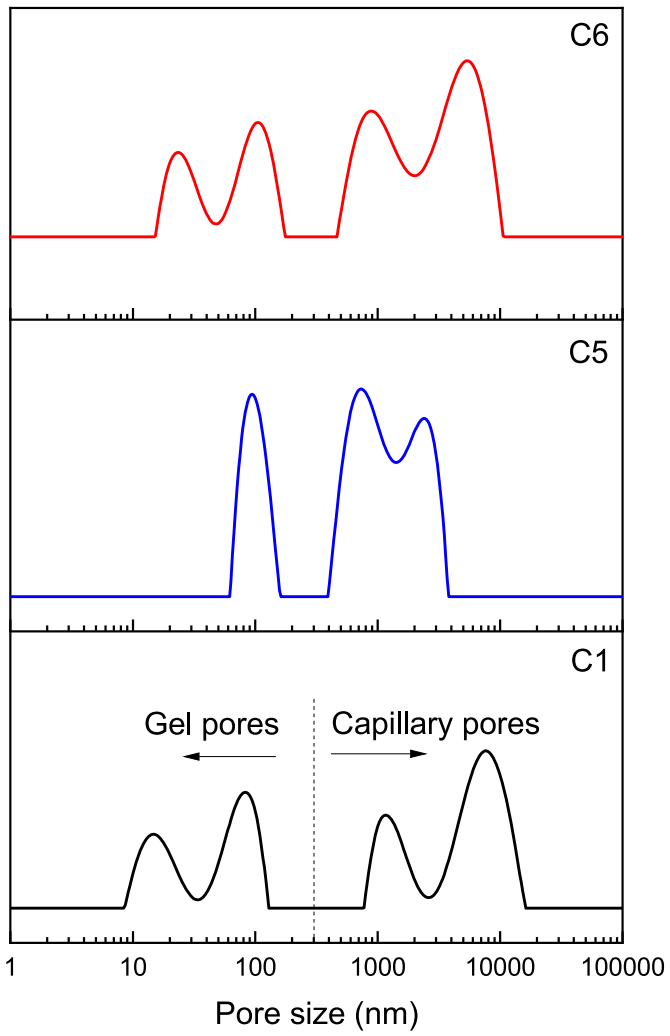

Fig. 8. The pore size distributions in C1, C5 and C6.

3.5. NMR

Fig. 8 shows the pore size distributions in ternary binder pastes subjected to CO_2 curing (Other mixtures were not presented as they have similar curve shape as C1). For all mixtures, there are two types of pores. The pores with the size bigger than 200 nm correspond to capillary pores and the gel pores in silica-rich gel relate to the pores smaller than 200 nm. The porosity results of pastes as summarized in Table 3 show that the incorporation of FA decreased the porosity. For instance, the porosity of C1 was 16.4%. While it decreased to 15.4% and 15.0% when incorporating 25% and 50% of FA, respectively. However, the addition of GGBS increased the porosity. As can be seen, the porosity of pastes incorporating 25% and 50% of GGBS were 29.0% and 33.4%, respectively.

3.6. SEM-BSE

Fig. 9 shows the SEM images of C1, C5 and C6 after CO2 curing. Fig. 9 (a) and (b) show that the PC was fully covered by inflorescence-like calcium carbonate particles with the particle size of 2 μm. When adding FA (Fig. 9 (c) and (d)), hexagonal calcium carbonate was formed both on the surface of FA and in the matrix of paste. The grain size of the crystalline calcium carbonate was about 1 μm. Some rod-like phase in C5 might be gypsum, as demonstrated by EDX results. Fig. 9 (e) and (f) show the SEM pictures of C6, which incorporated 50% of GGBS. Compared to the cement particles, GGBS was not fully covered by calcium carbonate. The particle size (0.5 μm) of calcium carbonate was much smaller than that in pure paste.

Fig. 10 shows the BSE images of CO_2-cured pastes. In C1 sample, a rim can be observed around PC particles which had a Ca/Si molar ratio of 1.2 according to the EDX results. The Ca/Si molar ratio of these rims was much lower than that in the matrix, which was about 6.7. Fig. 10 (c) and (d) exhibit the surface of FA and GGBS, which do not appear to be connected with the surrounding matrix. No rim was observed around FA or GGBS particles, suggesting that they did not react during the CO2 curing process, which will be further discussed in section 4. This weak interfacial transition zone (ITZ) between the matrix and unreacted FA and GGBS particles may lead to coarser and weaker bonds that could ultimately result in reduced compressive strength.

3.7. TEM

TEM images revealed a granule-shaped calcite (see Fig. 11 (a)) and a thin lath-shaped vaterite morphology (see Fig. 11 (c)) for the carbonation products in C1 sample. This was determined based on the d-space calculation from the high-resolution transmission microscopy (HRTM) lattice images as shown in Fig. 11 (b) and (d). Vaterite was not observed according to the XRD spectrum, which might be due to its low concentration. Both calcite and vaterite were surrounded by a thin (around 3 nm) amorphous layer. Other studies also noticed the formation of a single and thin (few tens of nanometers) layer rich of silicon [31]. However, it was not possible to perform EDS on this layer due to its thinness. As a result, it is hypothesized that this layer is silica-rich gel. In previous study conducted by Park et al. [27], it was reported that the rim (about several micrometer) surrounding calcium silicate consisted of Ca-modified silica gel. However, the amorphous layer in our study was considerably thinner compared to the rim depicted in the SEM images of [27]. This suggests that the rim not only contained silica-rich gel, but also crystal calcium carbonate. Fig. 11 (e) and (g) revealed the TEM image of calcite in C5 near FA particles and C6 near GGBS particles. In contrast to the products observed in C1, both samples displayed a sheet-like morphology and were not surrounded by an amorphous layer. This suggests that calcite deposited on the surface of FA and GGBS rather than being formed through the carbonation of FA or GGBS. Besides, C5 revealed a porous structure (Fig. 11 (f)) compared to the products in C1 (Fig. 11 (b) and (d)). The formation of nanopores might be one of the reasons that the blended pastes showed a lower compressive strength compared to the reference one. The plane spacing value of calcite in C1 at (2 1 0) lattice plane (main peak) was 0.3028 nm, while this value in C5 and C6 was 0.3036 nm and 0.3034 nm, respectively. The plane spacing of calcite in the latter two samples were very close to that of the standard calcite, i. e. 0.3035 nm [28]. This suggests that the calcite formed in C5 and C6 were well-crystallized. The addition of FA and GGBS were in favor of the improvement of crystallinity of calcite.

4. Discussions

Based on the results in Table 3, the ternary contour figures were plotted in Fig. 12. The relationship between the responses and mixture proportions was solved and presented in Table 6, which can be used to predict the properties of this ternary binder cement.

As discussed previously, FA and GGBS were relatively unreacted during the CO_2-curing process as demonstrated by BSE images. FA was not carbonated due to its low calcium content. Monkman and Shao. [29] reported a similar observation regarding the relatively unreactive nature of GGBS toward carbonation. This was based on their finding that the CO_2 uptake of pure GGBS was only 5%. One possible reason for the limited carbonation of GGBS could be attributed to its lower reactivity and calcium content (Table 1) as compared to PC [29]. Consequently, carbonation of clinker particles was prioritized over GGBS during this 3h-curing period. Besides, calcite particles precipitated on the surface of GGBS, which was known to inhibit further carbonation by passivating

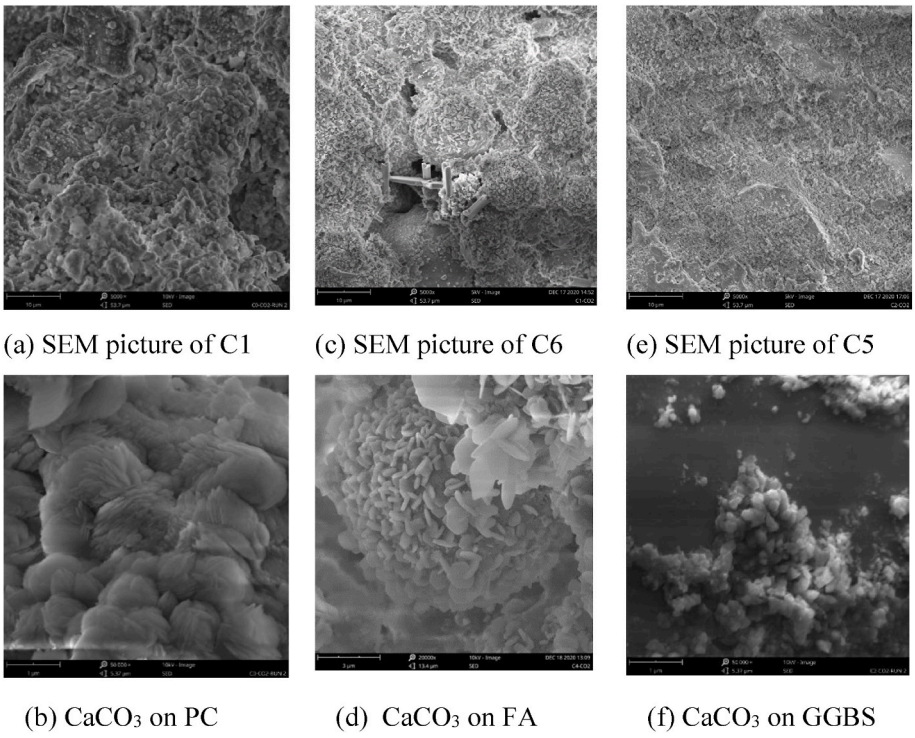

Fig. 9. SEM images and EDX results of C1, C5 and C6.

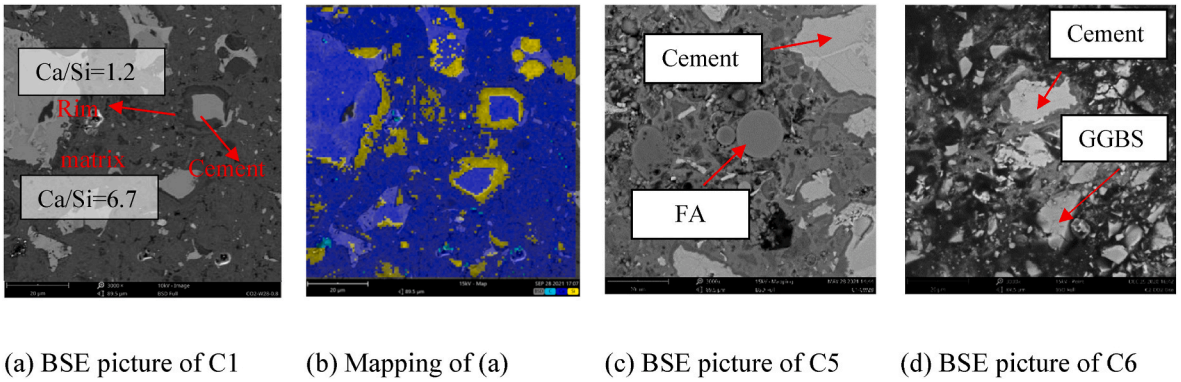

Fig. 10. BSE images and EDX results of C1, C5 and C6.

the surface [30]. This passivation effect may further contribute to the observed unreacted particles. Even though they were not carbonated, they increased the carbonation degree of cement as can be seen from Fig. 12 (a). Besides, the carbonation degree increased with the increase of FA content when the PC content was constant, which means that FA showed more obvious effect on the improvement of the carbonation degree. This is in agreement with the literatures showing that the incorporation of 50% of FA increased the CO_2 uptake by about 10% [10] and the addition of GGBS led to the increase of the carbonation efficiency [31]. The reason for this increase might be due to the filler effect as described below.

First, the water to cement ratio increased due to the addition of FA and GGBS. Since the carbonation can only occur with the presence of water, the increase of water content could consequently promote the carbonation reaction of cement [32]. Second, the incorporation of FA and GGBS provided extra space for the carbonation of cement. As mentioned above, the carbonation products formed a dense layer around cement particles and inhibited further carbonation. Due to the dilution effect of FA and GGBS, there was more extra space for the formation of carbonation products [33]. Therefore, the carbonation was accelerated. Third, the SEM images showed the participation of calcite on FA and GGBS indicating FA and GGBS providing more nucleation sites for the growth of calcite crystals [23]. This seed effect of FA/GGBS during the nucleation of calcite could also facilitate the formation of crystals and the improvement of the calcite crystallinity. Moreover, the distance between the surface of particles was decreased due to the addition of fine particles in cement, such as GGBS. This resulted in a shorter path for the diffusion of chemical species and promoted the dissolution of cement [34].

The morphology of calcite formed in pure cement and GGBS-blended cement was rhombohedral shaped. By contrast, the calcite precipitated on FA particles was hexagonal plate shaped. This is related to the difference of nucleation process of calcite in different systems. For pure cement paste, calcite was formed in pore solution, i.e., homogeneous nucleation. Therefore, the crystalline surface grows by the spreading of single layers, or equivalently, by the lateral advance of the growth steps bounding the layers as shown in Fig. 13(a). When adding FA particles, calcite precipitated on these spherical particles. To grow on this

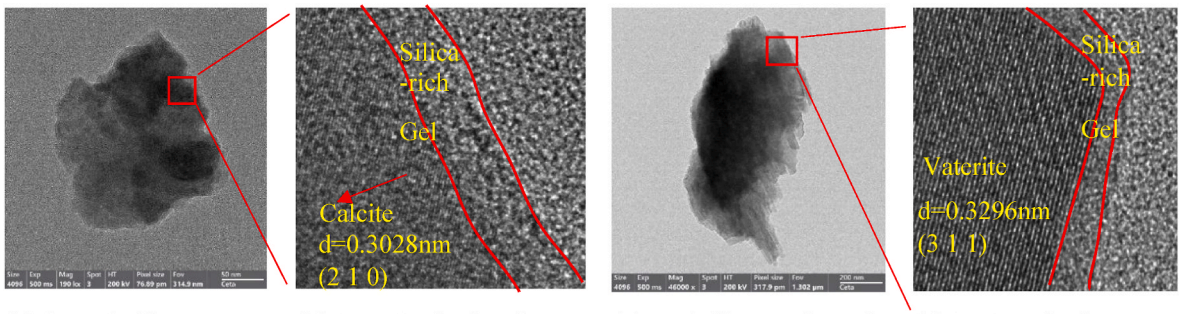

(a)Granule like products in C1 (b) HRTM lattice image of (a) (c) Lath like products in C1 (d) HRTM lattice image of (c)

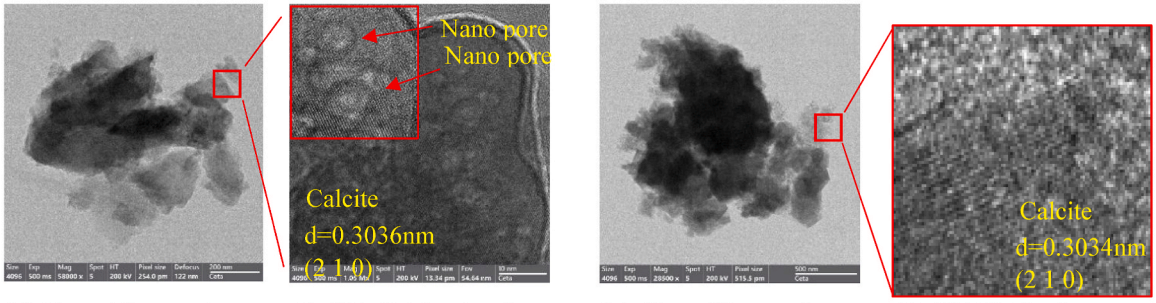

(e) Sheet like products in C5 (f) HRTM lattice image of (e) (g) Sheet like products in C6 (h) HRTM lattice image of (g)

Fig. 11. TEM images of C1, C5 and C6.

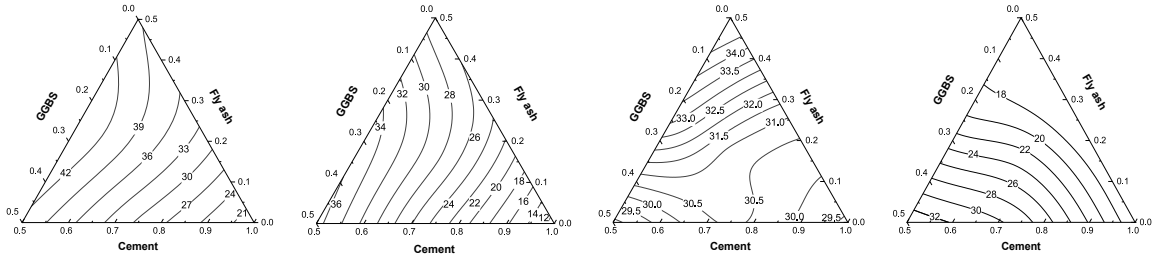

(a) Carbonation degree (%) (b) Calcite content (%) normalized with respect to the PC content (c) Crystal size (nm) of calcite (d) Porosity (%)

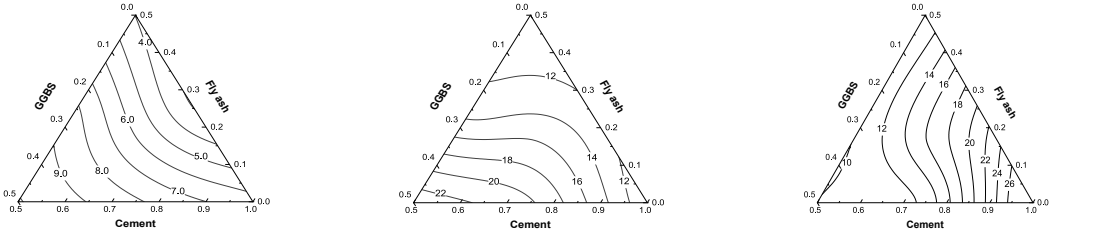

(e) Gel pore percentage (%) (f) Capillary pore percentage (%) (g) Compressive strength (MPa)

Fig. 12. Contour analysis of the ternary binder pastes.

spherical substrate, the (1,0,0) plane of calcite crystal rotated and formed hexagonal plate shape [35] due to its lower nucleation barrier as shown in Fig. 13(c). This can be explained as following.

It is commonly understood that the nucleation barrier or the change of Gibbs free energy (ΔG_S) can be calculated as:

$$\Delta G_S = \gamma_{LX} A_{LX} + \gamma_{XS} A_{XS} + \gamma_{LS} A_{LS} \quad (20)$$

Where γ_{LX}, γ_{XS}, and γ_{LS} are the interfacial energy of liquid-nucleus, nucleus-solid, and liquid-solid interface. A_{LX}, A_{XS}, and A_{LS} are the interfacial area of these three interfaces.

Table 6
The relationship between responses and mixture proportions.

Responses	Equations
Carbonation degree	$Y = 19.1X_1 + 22.6X_2 + 70.3X_3 + 73.8X_1X_2 - 13.2X_1X_3 + 56.6X_2X_3 + 36.8X_1X_2X_3$ (13)
Calcite content	$Y = 10.9X_1 - 14.5X_2 + 78.7X_3 + 109.6X_1X_2 - 31.2X_1X_3 - 100.7X_2X_3 + 313.3X_1X_2X_3$ (14)
Crystal size of calcite	$Y = 294X_1 + 528X_2 + 154X_3 - 232X_1X_2 + 256X_1X_3 + 1322X_2X_3 - 2277X_1X_2X_3$ (15)
Porosity	$Y = 16.4X_1 + 16.1X_2 + 17.9X_3 - 4.9X_1X_2 + 65.1X_1X_3 - 171.9X_2X_3 + 220.3X_1X_2X_3$ (16)
Gel pore percentage	$Y = 6.5X_1 + 21.1X_2 + 13.9X_3 - 39.2X_1X_2 - 0.8X_1X_3 + 53.2X_2X_3 - 64.7X_1X_2X_3$ (17)
Capillary pore percentage	$Y = 9.9X_1 - 5.0X_2 + 4.0X_3 + 34.3X_1X_2 + 65.9X_1X_3 - 232.7X_2X_3 + 296.6X_1X_2X_3$ (18)
Compressive strength	$Y = 30.4X_1 - 10.6X_2 + 51X_3 + 0.8X_1X_2 - 122.4X_1X_3 - 234X_2X_3 + 480.8X_1X_2X_3$ (19)

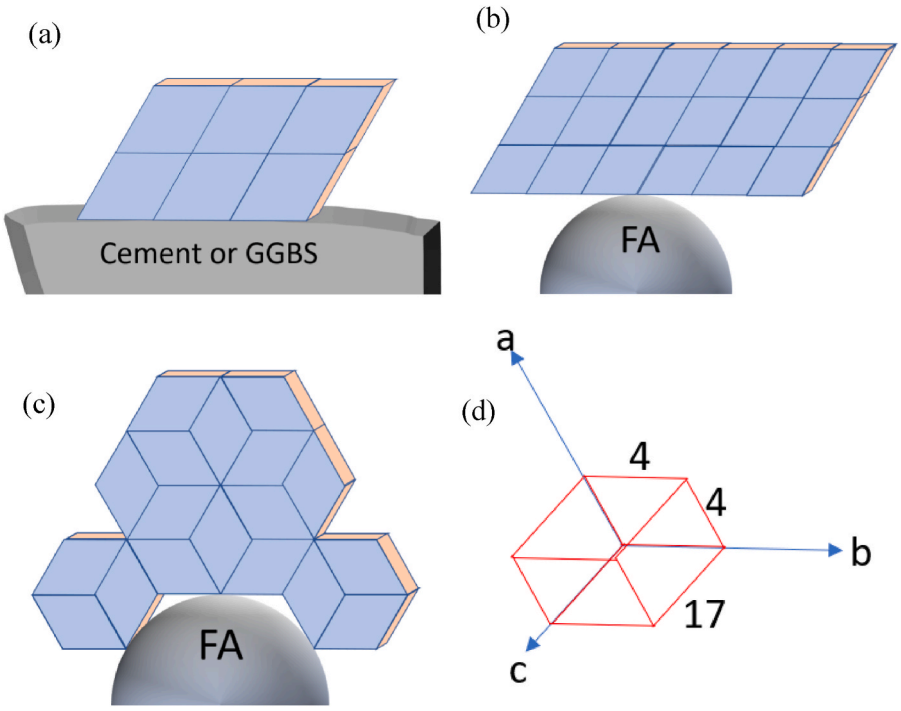

Fig. 13. Schematic illustration for the formation of calcite on different raw materials and crystal cell of calcite.

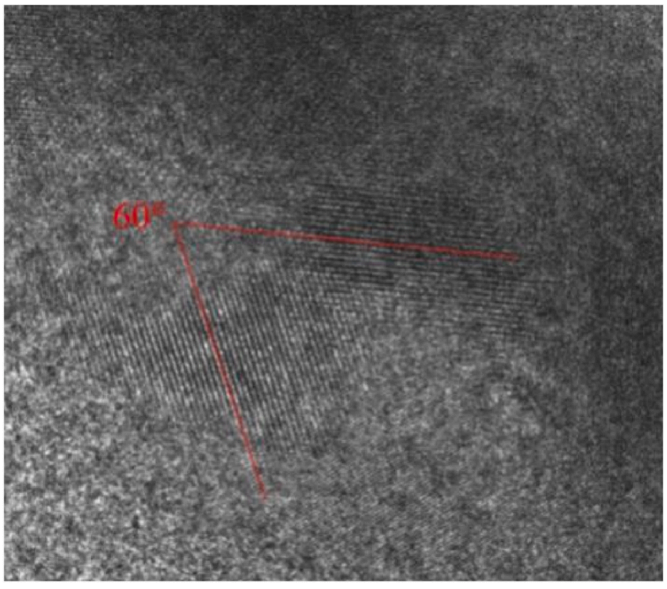

Fig. 14. The TEM image of C5 showing the angel between crystal planes.

Assuming 18 calcite crystals grow by the spreading of single layers on FA particles as shown in Fig. 13(b) and the interface between calcite and FA particle is 0, then:

$$\Delta G_S = \gamma_{LX} \times \left(4 \times \sqrt{3} \times 18 \times 2 + 17 \times 4 \times 18\right) = \gamma_{LX} \times \left(144\sqrt{3} + 1224\right) \tag{21}$$

when a = 4, b = 4 and c = 17 as shown in Fig. 13(d) based on its crystal structure.

When these 18 crystals rotate and form a hexagonal plate shape and the gap between calcite and FA particle is filled as shown in Fig. 13(c), the

$$\begin{aligned}\Delta G_S' &= \gamma_{LX} \times \left(4 \times \sqrt{3} \times 18 \times 2 + 17 \times 4 \times 16\right) + (17 \times 4 \times 4) \times (\gamma_{XS} - \gamma_{LS}) \\ &= \gamma_{LX} \times \left(144\sqrt{3} + 1088\right) + 272(\gamma_{XS} - \gamma_{LS})\end{aligned} \tag{22}$$

Normally, γ_{LS} is higher than γ_{XS}. Therefore, $\Delta G_S'$ is less than ΔG_S and calcite tend to form as a hexagonal shape on FA particles.

The rotation of crystal planes in FA-blended sample can also be found on the high-resolution image of TEM test as shown in Fig. 14. The surface of GGBS was flat, thus there was no rotation of calcite plane. This the reason that the calcite on GGBS particles were still rhombohedral

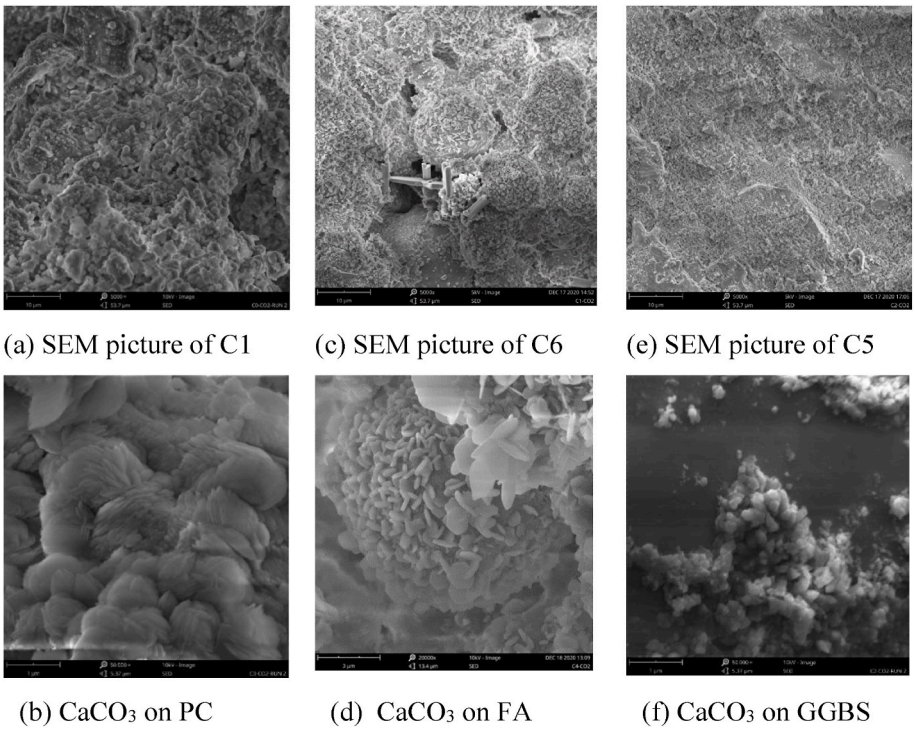

Fig. 15. Main mineralogical compositions (%) of PC and pastes normalized with respect to the PC content.

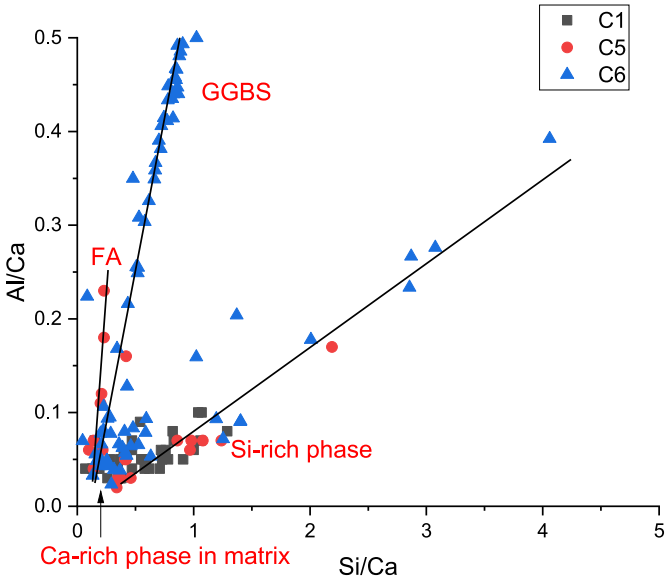

Fig. 16. EDS points analysis for C1, C5 and C6.

shaped as shown in Fig. 13(a).

To better understand the effect of FA and GGBS on the carbonation of cement particles, the alite, belite, and calcite content in blended pastes was normalized by PC and the result is summarized in Fig. 15. The amorphous content was calculated by subtracting the amorphous content of FA and GGBS assuming that FA and GGBS didn't react with CO_2. It shows that the contents of alite and belite decreased, while the calcite content significantly increased with the incorporation of FA and GGBS. This indicates that the incorporation of FA or GGBS promoted the formation of calcite and reduced the unreacted PC content due to the filler effect mentioned above. Based on the results in Fig. 15, the ternary contour of calcite content can be plotted. Fig. 12(b) shows that the incorporation of FA and GGBS had similar effect on increasing the calcite content.

As shown in Fig. 12(c), the incorporation of FA increased the crystal size of calcite. This may relate to the heterogeneous nucleation of calcite. It was assumed that the surface of cement is flat. The barrier energy to nucleation was higher for spherical substrate (the surface of fly ash) than a flat substrate (the surface of cement) [36]. Therefore, the nucleation rate on the surface of cement was higher and thus the crystal size of calcite was smaller than that on FA. On the other hand, GGBS decreased the crystal size of calcite. This may relate to the high Mg content in GGBS, as indicated in Table 1. Previous studies have demonstrated that Mg^{2+} ions inhibited the formation of calcite, resulting in a decrease of its crystal size [37]. Based on Table 1, the MgO content in GGBS was approximately 9%, which could be the cause for the reduction in crystal size of calcite. Even though, GGBS still showed a more obvious effect on the increase of calcite content. This might be related to the higher nucleation rate [38] as mentioned above and the lower particle size of GGBS that proving higher specific surface area compared to that of FA.

Based on the calculation of plane spacing value, the calcite formed in CO_2-cured samples has crystal defect. On the contrary, the calcite formed in FA/GGBS-blended samples has higher crystallinity. The TG spectra also showed that the calcium carbonated in cement incorporating FA has higher decomposition temperature compared to the reference cement. This indicates that the addition of FA or GGBS were in favor of the improvement of crystallinity of carbonation products. This may be related to the seed effect of FA/GGBS during the nucleation of calcite that facilitated the formation of crystals [39].

According to Fig. 16, the Al/Si ratio of silica-rich gel remained at around 0.09 regardless of whether pure cement or FA/GGBS blended cement was used. This indicates that the silica-rich gel had a low amount of Al even when Al-rich admixture like FA and GGBS were used. This finding supports the previous discussion that FA and GGBS were relatively unreacted in the mixture. Calcium carbonate was located in the left corner of Fig. 16, but it cannot be separated completely from silica-rich gel. This is because calcium carbonate and silica-rich gel were interlocked tightly when they were produced. The silica-rich phase was

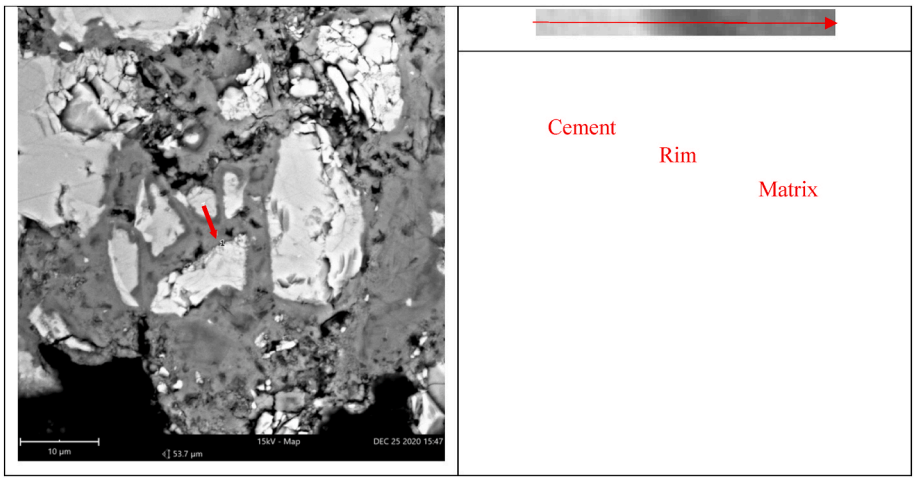

Fig. 17. EDS line scan spectra from cement particle to the cement matrix.

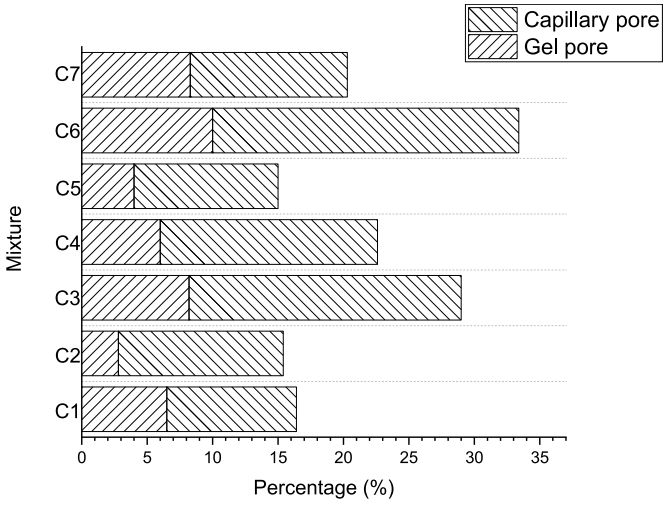

Fig. 18. The capillary pore and gel pore percentage in cement paste.

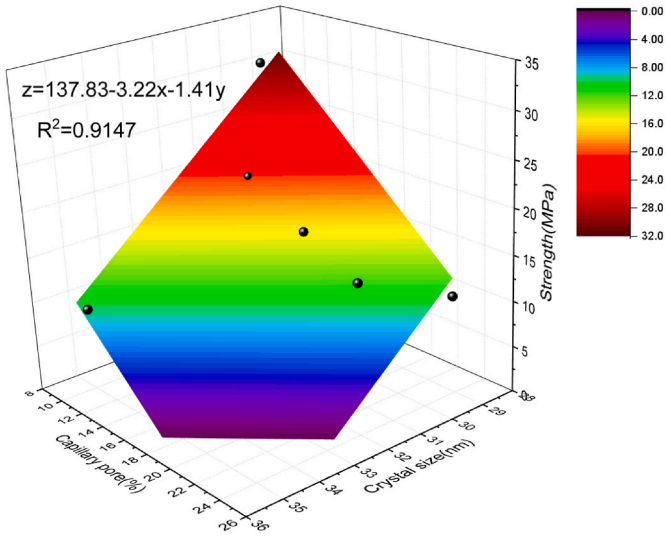

Fig. 19. Regression prediction for compressive strength, crystal size of calcite and capillary pore percentage.

Table 7
MLR analysis results of compressive strength.

	Coefficient	Standard Error	t-Value	Prob> |t|
Intercept	155.0	26.31	5.91	0.027
Crystal size	−3.35	0.61	−5.49	0.032
CO_2 uptake	−1.05	1.13	−0.93	0.451
Capillary pores	−1.14	0.34	−3.35	0.079
Gel pores	−0.86	0.71	−1.20	0.352

mainly located near to the cement particles while the calcium-rich phase was mainly located in the matrix as shown in Fig. 17. From Fig. 16, it can also be seen that the silica-rich phase in the sample incorporating GGBS and FA showed higher Si/Ca ratio than that in pure cement. One possible explanation for this observation is that the acceleration effect of GGBS and FA on the carbonation facilitated the decalcification of cement clinkers.

Despite the fact that GGBS and FA increased the content of calcite, the compressive strength deceased with the increase of GGBS or FA content as shown in Fig. 12(g). Shao et al. [29] also reported that the strength of CO_2-cured GGBS or FA paste was much lower than that of CO_2-cured cement paste. The decreasing effect of GGBS might be due to the porosity. As can be seen from Fig. 12 (d), the incorporation of GGBS increased the porosity of paste. This was in line with the results shown in Ref. [31] about carbonation of GGBS concrete. FA-blended paste showed lower porosity than pure cement paste, but it decreased the compressive strength as well. This might be due to the difference of the calcite morphology. The carbonation products in pure cement paste were connected with each other and formed a dense structure. While the calcite particles in FA-blended cement paste were dispersed around FA particles, thus forming a loose structure as shown in SEM pictures. Moreover, the higher crystal size and nanopores on calcite, as demonstrated by TEM images, might be another reason for the decrease of compressive strength of FA/GGBS-blended cement.

The capillary pore and gel pore percentages were calculated and presented in Fig. 18. With the incorporation of GGBS (C3 and C6), the capillary pore and gel pore percentages increased. On the contrary, these values decreased with the incorporation of FA (C2 and C5). The contour analysis in Fig. 12 (e) and (f) also proved the coarsening effect of GGBS and the refining effect of FA. As a result, GGBS showed more negative effect on the decreasing of compressive strength compared to FA as shown in Fig. 12 (g).

Multiple linear regression (MLR) was adopted to better understand the relationship between compressive strength and other parameters such as porosity, crystal size and CO_2 uptake. MLR is a linear statistical technique to predict the best relationship between a dependent variable and several independent variables. A general MLR model is shown in Eq. (23):

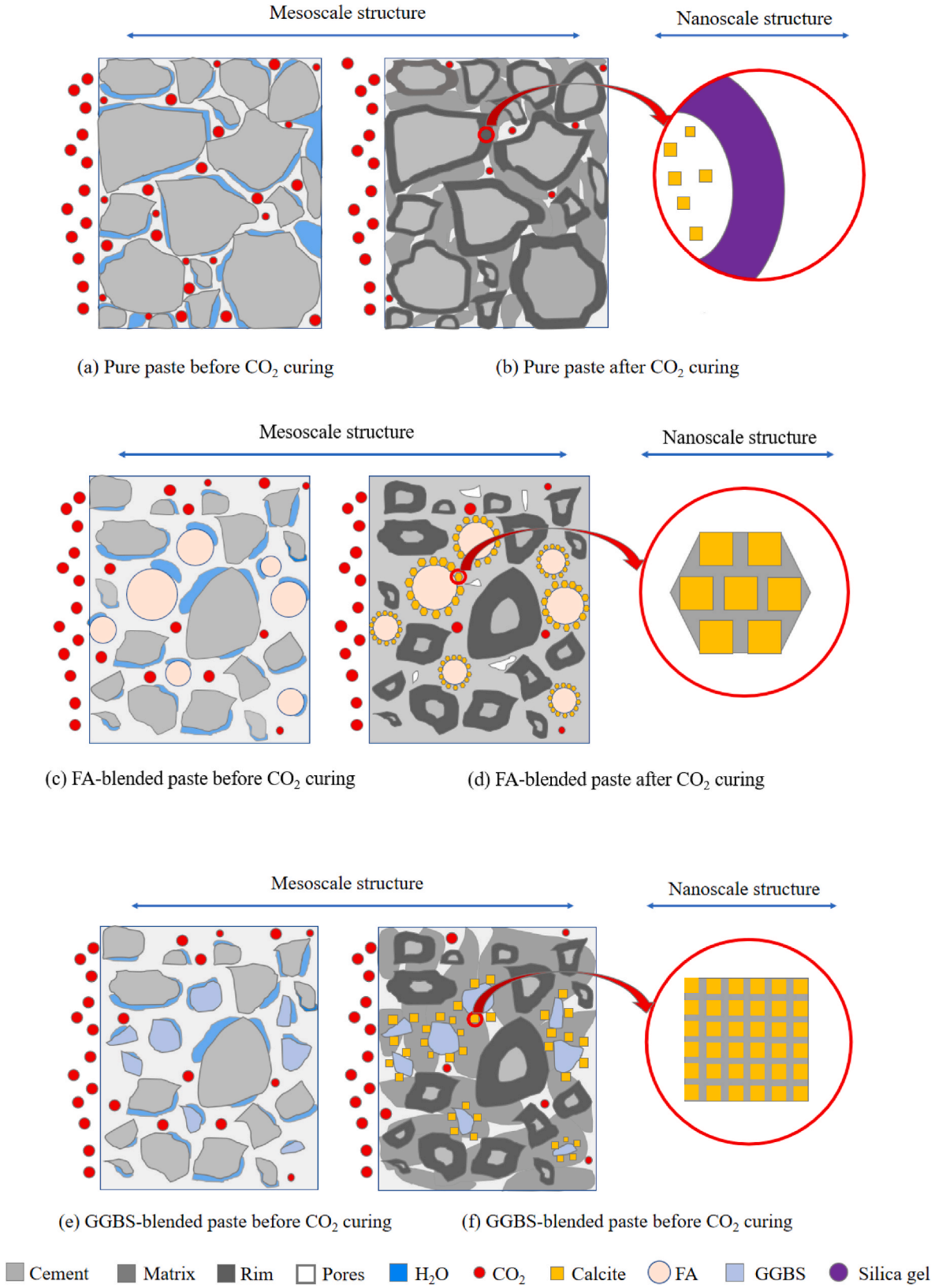

Fig. 20. A schematic diagram of the effect of FA and GGBS on the CO_2 curing process.

$$Y = \beta_0 + \beta_1 X_1 \ldots + \beta_n X_n \quad (23)$$

Where Y indicates dependent variable, X_i represents independent variables, β_i represents predicted parameters.

In this study, crystal size of calcite, CO_2 uptake, capillary pores and gel pores were considered as independent variables. The MLR analysis results are shown in Table 7. It can be seen that the P-values of CO_2 uptake and gel pores are much higher than 0.05, indicating that these two variables had no significant effect on the compressive strength. When CO_2 uptake was removed from MLR, the P-value of gel pores (0.45) was still high. Therefore, CO_2 uptake and gel pores were not considered for MLR analysis. Then, the P-values of crystal size and capillary pores were changed to 0.00479 and 0.0045 respectively, indicating their significant effect on the compressive strength. The relationship between strength and these two variables is shown as follows:

$$Y = 137.83 - 3.22X_1 - 1.41X_2 \quad (24)$$

Where Y indicates the compressive strength of ternary binder system, X_1 and X_2 represent the crystal size of calcite and capillary pores respectively.

The regression analysis results were plotted in Fig. 19. The R^2 value of 0.914 shows a good correlation between measured compressive strength and estimated strength. The negative coefficients for the crystal size of calcite and capillary pores suggest that an increase in their size will result in a reduction in strength. Numerous studies have reported the linear relationship between porosity and compressive strength of hardened concrete [40]. But the R^2 value was quite low (0.23) when porosity was included only for the linear regression. This is because the morphology and crystal size of calcite changed with the addition of FA and GGBS. The crystal size increased with the addition of FA, which also contributed to the decrease of the compressive strength. This is consistent with the results in Ref. [41], which showed the crystals with smaller size are stronger.

Based on the results of this study, a schematic diagram illustrating the impact of FA and GGBS on calcite precipitation, calcite content, crystal size and porosity in the CO_2-cured samples was drawn (Fig. 20). During the CO_2 curing of pure cement paste, CO_2 reacted with cement particle and formed calcium carbonate and silica-rich gel. The matrix and rim encompassing the cement particles contained both calcium carbonate and silica-rich gel. But the former was mainly in the matrix, while the latter was mainly in the rim. Besides, calcium carbonate crystals were surrounded by amorphous layer. In FA/GGBS-blended cement, FA or GGBS remained unreacted and calcium carbonate precipitated on FA and GGBS. As a result, the incorporation of FA and GGBS increased the carbonation degree and the calcite content. The calcite precipitated on FA particles were hexagonal plate, while that on GGBS particles and cement particles were small rhombohedral crystals. FA decreased the porosity, capillary pore and gel pore percentages of carbonated cement, while GGBS had opposite effect.

5. Limitations

This manuscript studied the influential mechanism of FA and GGBS on the properties of CO2-cured cement. However, there are a few limitations in this study. During pre-conditioning process, hydration of PC occurred, and a small amount of hydration products formed. However, the competition between carbonation and hydration of cement and the kinetics of reactions were not discussed in this study. It should also be noted that the addition of GGBS and FA may not only affect the properties and microstructures of paste during CO_2 curing process, but also affect the further hydration of PC due to the pozzolanic reaction. This effect will be presented in the subsequent study.

Besides, pure CO_2 at high pressure was used in this study, which may not accurately reflect the conditions of real carbonation. The use of waste fuel gas with normal pressure could be a more cost-effective approach in further studies. However, it's worth noting that using waste fuel gas may also introduce additional impurities and contaminants that could potentially impact the properties of cement-based materials.

Overall, while the study provides valuable insights into the effects of short-term (3h) CO_2 curing on the cement matrix immediately after casting, it is important to acknowledge these limitations and consider further research that could address them. This would enable a more comprehensive understanding of the complex processes involved in carbonation and its impact on cement-based materials.

6. Conclusions

Based on the obtained results in this study, the following conclusions can be drawn:

(1) FA and GGBS particles were not carbonated in the CO_2-cured cement samples. However, the incorporation of FA and GGBS increased significantly the carbonation degree of cement particles and calcite content due to the filler effect. FA showed more effect on the increase of carbonation degree of cement.
(2) The morphology of calcite precipitated on FA and GGBS particles were different. The calcite formed on cement particles was surrounded by an amorphous silica-rich gel layer, while the one on FA or GGBS particles has no amorphous layer. The calcite on FA particles was hexagonal plate shaped, while the one on GGBS and cement particles was rhombohedral shaped. The addition of FA and increased the crystallinity of calcite due to the nucleation effect. FA increased the crystal size (nano scale) of calcite, while GGBS showed opposite effect. But the particle size (micro scale) of calcite decreased with the incorporation of FA or GGBS.
(3) The incorporation of FA or GGBS decreased the compressive strength of the CO_2-cured mortars due to the loose microstructure and the nanopores on the carbonation products. The capillary pore percentage and the crystal size of calcite had significant negative effect on the compressive strength. GGBS showed more obvious negative effect on the decrease of strength than FA due to the higher porosity.

Declaration of competing interest

The authors declare that they have no known competing financial interests or personal relationships that could have appeared to influence the work reported in this paper.

Data availability

Data will be made available on request.

Acknowledgements

The authors would like to acknowledge the financial support from National Natural Science Foundation of China grant numbers 52050410333, 52078204 and National Natural Science Foundation of Hunan province grant number 2021RC2063.

References

[1] B. Lu, C. Shi, G. Hou, Strength and microstructure of CO_2 cured low-calcium clinker, Construct. Build. Mater. 188 (2018) 417–423, https://doi.org/10.1016/j.conbuildmat.2018.08.134.
[2] D. Wang, J. Chang, Comparison on accelerated carbonation of β-C_2S, $Ca(OH)_2$, and C_4AF: reaction degree, multi-properties, and products, Construct. Build. Mater. 224 (2019) 336–347, https://doi.org/10.1016/j.conbuildmat.2019.07.056.
[3] Z. Liu, W. Meng, Fundamental understanding of carbonation curing and durability of carbonation-cured cement-based composites: a review, J. CO2 Util. 44 (2021), https://doi.org/10.1016/j.jcou.2020.101428.

[4] X. Pan, C. Shi, N. Farzadnia, X. Hu, J. Zheng, Properties and microstructure of CO_2 surface treated cement mortars with subsequent lime-saturated water curing, Cement Concr. Compos. 99 (2019) 89–99, https://doi.org/10.1016/j.cemconcomp.2019.03.006.

[5] M. Mahoutian, Y. Shao, Production of cement-free construction blocks from industry wastes, J. Clean. Prod. 137 (2016) 1339–1346, https://doi.org/10.1016/j.jclepro.2016.08.012.

[6] T. Bremner, P. Eng, Environmental aspects of concrete: problems and solutions, in: All-Russian Conference on Concrete and Reinforced Concrete, 2001.

[7] S. Cheng, Z. Shui, T. Sun, R. Yu, G. Zhang, Durability and microstructure of coral sand concrete incorporating supplementary cementitious materials, Construct. Build. Mater. 171 (2018) 44–53, https://doi.org/10.1016/j.conbuildmat.2018.03.082.

[8] M.F. Alnahhal, U.J. Alengaram, M.Z. Jumaat, B. Alsubari, M.A. Alqedra, K.H. Mo, Effect of aggressive chemicals on durability and microstructure properties of concrete containing crushed new concrete aggregate and non-traditional supplementary cementitious materials, Construct. Build. Mater. 163 (2018) 482–495, https://doi.org/10.1016/j.conbuildmat.2017.12.106.

[9] C. Shi, M. Liu, P. He, Z. Ou, Factors affecting kinetics of CO_2 curing of concrete, Journal of Sustainable Cement-Based Materials 1 (1–2) (2012) 24–33, https://doi.org/10.1080/21650373.2012.727321.

[10] D. Zhang, X. Cai, Y. Shao, Carbonation curing of precast fly ash concrete, J. Mater. Civ. Eng. 28 (11) (2016), 04016127, https://doi.org/10.1061/(ASCE)MT.1943-5533.0001649.

[11] D. Zhang, Y. Shao, Effect of early carbonation curing on chloride penetration and weathering carbonation in concrete, Construct. Build. Mater. 123 (2016) 516–526, https://doi.org/10.1016/j.conbuildmat.2016.07.041.

[12] L. Qin, X. Gao, T. Chen, Influence of mineral admixtures on carbonation curing of cement paste, Construct. Build. Mater. 212 (2019) 653–662, https://doi.org/10.1016/j.conbuildmat.2019.04.033.

[13] Y. Wang, B. Lu, X. Hu, J. Liu, Z. Zhang, X. Pan, Z. Xie, J. Chang, T. Zhang, M. L. Nehdi, C. Shi, Effect of CO_2 surface treatment on penetrability and microstructure of cement-fly ash–slag ternary concrete, Cement Concr. Compos. 123 (2021), https://doi.org/10.1016/j.cemconcomp.2021.104194.

[14] China National Standards GB 8076, Standard for Concrete Admixture, 2008. Beijing, China (in Chinese).

[15] D. Jiao, C. Shi, Q. Yuan, X. An, Y. Liu, Mixture design of concrete using simplex centroid design method, Cement Concr. Compos. 89 (2018) 76–88, https://doi.org/10.1016/j.cemconcomp.2018.03.001.

[16] E. Dougla, G. Pouskouleli, Prediction of compressive strength of mortars made with portland cement - blast-furnace slag - fly ash blends, Cement Concr. Res. 21 (4) (1991) 523–534, https://doi.org/10.1016/0008-8846(91)90102-N.

[17] Z. Shi, C. Shi, R. Zhao, D. Wang, F. He, Factorial design method for designing ternary composite cements to mitigate ASR expansion, J. Mater. Civ. Eng. 28 (9) (2016), https://doi.org/10.1061/(asce)mt.1943-5533.0001568.

[18] D. Wang, Z. Chen, On predicting compressive strengths of mortars with ternary blends of cement, ggbfs and fly ash, Cement Concr. Res. 27 (1997) 487–493, https://doi.org/10.1016/S0008-8846(97)00039-2.

[19] P. He, C. Shi, Z. Tu, C.S. Poon, J. Zhang, Effect of further water curing on compressive strength and microstructure of CO_2-cured concrete, Cement Concr. Compos. 72 (2016) 80–88, https://doi.org/10.1016/j.cemconcomp.2016.05.026.

[20] H.H. Steinour, Some effects of carbon dioxide on mortars and concrete-discussion, Journal of American Concrete Institution 30 (2) (1959) 905–907.

[21] A. Valori, P.J. McDonald, K.L. Scrivener, The morphology of C–S–H: lessons from 1H nuclear magnetic resonance relaxometry, Cement Concr. Res. 49 (2013) 65–81, https://doi.org/10.1016/j.cemconres.2013.03.011.

[22] X. Hu, C. Shi, D. Zhu, G. De Schutter, Investigation on influential factors on chloride concentration index of cement-based materials by pore solution expression method, Construct. Build. Mater. 231 (2020), 117135, https://doi.org/10.1016/j.conbuildmat.2019.117135.

[23] Z. Tu, M.-z. Guo, C.S. Poon, C. Shi, Effects of limestone powder on $CaCO_3$ precipitation in CO_2 cured cement pastes, Cement Concr. Compos. 72 (2016) 9–16, https://doi.org/10.1016/j.cemconcomp.2016.05.019.

[24] W. Ashraf, J. Olek, Elucidating the accelerated carbonation products of calcium silicates using multi-technique approach, J. CO2 Util. 23 (2018) 61–74, https://doi.org/10.1016/j.jcou.2017.11.003.

[25] M. Zajac, L. Irbe, F. Bullerjahn, H. Hilbig, M.B. Haha, Mechanisms of carbonation hydration hardening in Portland cements, Cement Concr. Res. 152 (2022), 106687.

[26] X. Zhang, H. Li, F. Hou, Y. Yang, H. Dong, N. Liu, Y. Wang, L. Cui, Synthesis of highly efficient Mn $_2$ O $_3$ catalysts for CO oxidation derived from Mn-MIL-100, Appl. Surf. Sci. 411 (2017) 27–33, https://doi.org/10.1016/j.apsusc.2017.03.179.

[27] Y. Mu, Z. Liu, F. Wang, X. Huang, Carbonation characteristics of γ-dicalcium silicate for low-carbon building material, Construct. Build. Mater. 177 (2018) 322–331, https://doi.org/10.1016/j.conbuildmat.2018.05.087.

[28] W.K. Park, S.-J. Ko, S.W. Lee, K.-H. Cho, J.-W. Ahn, C. Han, Effects of magnesium chloride and organic additives on the synthesis of aragonite precipitated calcium carbonate, J. Cryst. Growth 310 (10) (2008) 2593–2601, https://doi.org/10.1016/j.jcrysgro.2008.01.023.

[29] S. Monkman, Y. Shao, Assessing the carbonation behavior of cementitious materials, J. Mater. Civ. Eng. 18 (6) (2006) 768–776, https://doi.org/10.1061/(ASCE)0899-1561 (2006)18:6(768).

[30] C.S. Doyle, T. Kendelewicz, G.E. Brown Jr., Inhibition of the reduction of Cr (VI) at the magnetite–water interface by calcium carbonate coatings, Appl. Surf. Sci. 230 (1–4) (2004) 260–271.

[31] E. Gruyaert, P. Van den Heede, N. De Belie, Carbonation of slag concrete: effect of the cement replacement level and curing on the carbonation coefficient – effect of carbonation on the pore structure, Cement Concr. Compos. 35 (1) (2013) 39–48, https://doi.org/10.1016/j.cemconcomp.2012.08.024.

[32] S. Siddique, A. Naqi, J.G. Jang, Influence of water to cement ratio on CO_2 uptake capacity of belite-rich cement upon exposure to carbonation curing, Cement Concr. Compos. 111 (2020), https://doi.org/10.1016/j.cemconcomp.2020.103616.

[33] B. Lothenbach, K. Scrivener, R.D. Hooton, Supplementary cementitious materials, Cement Concr. Res. 41 (12) (2011) 1244–1256, https://doi.org/10.1016/j.cemconres.2010.12.001.

[34] E. Berodier, K. Scrivener, G. Scherer, Understanding the filler effect on the nucleation and growth of C-S-H, J. Am. Ceram. Soc. 97 (12) (2014) 3764–3773, https://doi.org/10.1111/jace.13177.

[35] H. Wei, Q. Shen, Y. Zhao, D. Wang, D. Xu, Crystallization habit of calcium carbonate in presence of sodium dodecyl sulfate and/or polypyrrolidone, J. Cryst. Growth 260 (3–4) (2004) 545–550.

[36] M. Iwamatsu, Line-tension effects on heterogeneous nucleation on a spherical substrate and in a spherical cavity, Langmuir 31 (13) (2015) 3861–3868, https://doi.org/10.1021/la504926s.

[37] H. Putra, H. Yasuhara, N. Kinoshita, D. Neupane, C.-W. Lu, Effect of magnesium as substitute material in enzyme-mediated calcite precipitation for soil-improvement technique, Front. Bioeng. Biotechnol. 4 (2016) 37.

[38] G.T. Kerr, Chemistry of crystalline aluminosilicates. I. Factors affecting the formation of zeolite A, J. Phys. Chem. 70 (4) (1966) 1047–1050, https://doi.org/10.1021/j100876a015.

[39] C.Y. Tai, J.-F. Wu, R.W. Rousseau, Interfacial supersaturation, secondary nucleation, and crystal growth, J. Cryst. Growth 116 (1992) 294–306, https://doi.org/10.1016/0022-0248(92)90636-W.

[40] C. Lian, Y. Zhuge, S. Beecham, The relationship between porosity and strength for porous concrete, Construct. Build. Mater. 25 (11) (2011) 4294–4298.

[41] R.W. Armstrong, 60 years of Hall-Petch: past to present nano-scale connections, Mater. Trans. 55 (1) (2014) 2–12.